CrossMark

A Holocene East Asian winter monsoon record at the southern edge of the Gobi Desert and its comparison with a transient simulation

Yu Li · Carrie Morrill

Abstract The East Asian winter monsoon (EAWM) exhibits significant variability on intraseasonal, interannual, and interdecadal time scales and the variability can be extended to Holocene centennial and millennial scales. Previous Holocene EAWM proxy data records, which were mostly located in Central, Eastern and Southern China, did not show a consistent Holocene EAWM history. Therefore, it is difficult to provide insights into mechanisms of the long-term winter monsoon variability on the basis of the records. Eolian sediments at the southern edge of the Gobi Desert, Western China, are sensitive to the EAWM changes and less affected by the East Asian summer monsoon due to an obstruction of the Qinghai–Tibet Plateau. This paper presents a comparison between a well-dated Holocene EAWM record and coupled climate model simulations, so as to explore physical processes and influencing factors of the Holocene EAWM. Sediment samples from two Holocene eolian sedimentary sections [Huangyanghe (a) and Huangyanghe (b)] were acquired at the southern edge of the Gobi Desert. Chronologies were established based on twenty bulk organic matter AMS ^{14}C ages and five pollen concentrates AMS ^{14}C ages. Proxy data, including grain-size, total organic carbon, magnetic susceptibility and carbonate content were obtained from the two eolian sections.

The grain-size standard deviation model was applied to determine components sensitive to variability of the Holocene EAWM. After a comparison of environmentally-sensitive grain-size components and proxy data, the 20–200 μm component at the Huangyanghe (a) and the 20–159 μm component at the Huangyanghe (b) section were selected as indicators of the Holocene EAWM, which show a strong early Holocene winter monsoon and a decline of the winter monsoon since the mid-Holocene. We also present equilibrium and transient simulations of the climate evolution for the Holocene using a state-of-art coupled climate model: the Community Climate System Model version 3 (CCSM3). Indices for the Holocene EAWM were calculated and are consistent with the reconstructed Holocene EAWM intensity. The simulations indicate that orbital forcing effects on the land-sea temperature and sea level pressure contrast can account for the observed EAWM trends. Other forcings that were present in the early Holocene, including the remnant Laurentide ice sheet and meltwater forcing in the North Atlantic, were not responsible for the Holocene trends.

Keywords East Asian winter monsoon · Holocene · Climate simulations · The Gobi Desert · Eolian sediments

Y. Li (✉)
College of Earth and Environmental Sciences, Center
for Hydrologic Cycle and Water Resources in Arid Region,
Lanzhou University, Lanzhou 730000, China
e-mail: oscaryoulee@gmail.com; liyu@lzu.edu.cn

Y. Li · C. Morrill
Paleoclimatology Branch, NOAA's National Climatic Data
Center, Boulder, CO 80305, USA

Y. Li · C. Morrill
University of Colorado, Boulder, CO, USA

1 Introduction

The East Asian winter monsoon (EAWM) generally refers to the atmospheric flow over Asia associated with the eastward and southward movement of cold air coming from the Siberian High, whose surges dominate the winter weather over East Asia and affect the Southern Hemisphere (SH) monsoon (Chang and Lau 1980; Ding and Krishnamurti 1987; Jhun and Lee 2004). It is well known that the modern
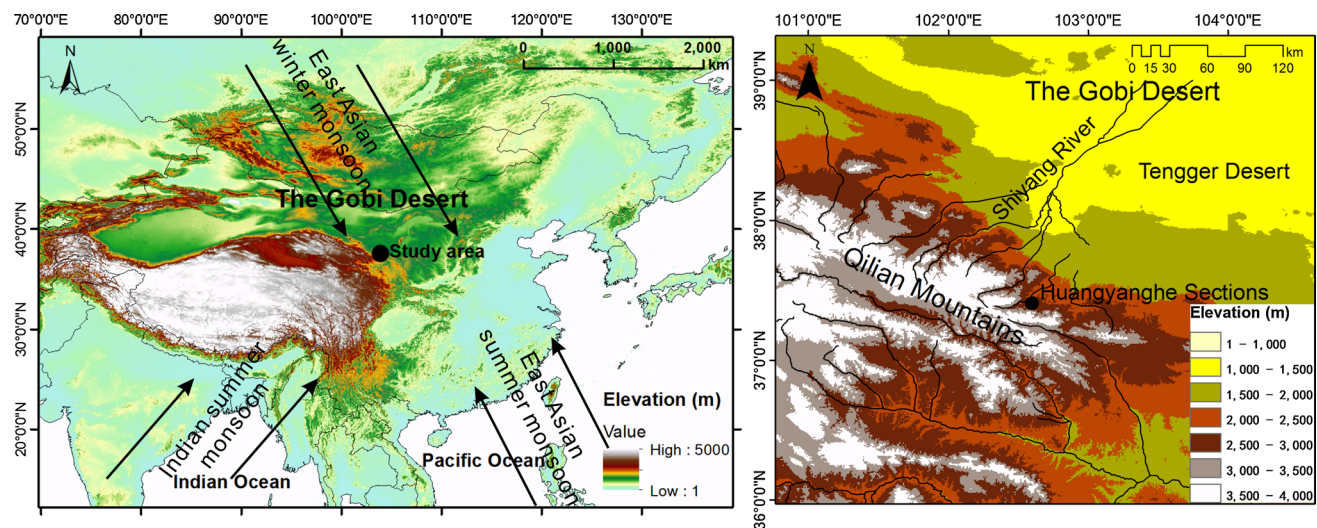
Fig. 1 Study area, the southern edge of the Gobi Desert, where the aeolian sediments are sensitive to EAWM changes

EAWM is closely linked to the Siberian high (Wu et al. 2002; Gong et al. 2001). In addition, there have been many efforts to describe its associations with the El Niño–Southern Oscillation (ENSO), physical geographic conditions on the Tibetan Plateau, Eurasian snow cover, the North Atlantic Oscillation (NAO), and the Arctic Oscillation (AO) (e.g., Chang and Lau 1982; Ding 1990; Zhang et al. 1997; Compo et al. 1999; Wang et al. 2000; Gong and Ho 2003; Jhun and Lee 2004; Yun et al. 2010). Modern variability of the EAWM has caused substantial social and economic losses, though it is still a challenge to predict the EAWM accurately due to lack of information about EAWM mechanisms on different time scales (Webster et al. 1998; Jhun and Lee 2004). Compared with modern EAWM observations and simulations, Holocene millennial-scale EAWM research is important in establishing baselines and is essential for determining amplitudes and rates in winter monsoon changes on a millennial timescale.

A number of studies have generated millennial-scale EAWM records since the 1990s (An et al. 1991; Xiao et al. 1995; An and Porter 1997; Lu et al. 2004; Yancheva et al. 2007; Wang et al. 2008, 2012; Yu et al. 2011; Sun et al. 2012). In these studies, different sediment types were successfully used to reconstruct the Holocene EAWM intensity, including eolian sediments (loess-paleosol sequences) (An et al. 1991; Yang and Ding 2008), lake sediments (Yancheva et al. 2007; Wang et al. 2008, 2012; Liu et al. 2009a) and marine sediments (Tian et al. 2010; Huang et al. 2011). Although many studies have been published concerning the Holocene EAWM evolution, proxy data scientists came to different conclusions on the winter monsoon history (Yancheva et al. 2007; Yang and Ding 2008; Wang et al. 2008, 2012; Yu et al. 2011; Huang et al. 2011). Therefore, it is still needed to develop a clear and

direct indicator for the Holocene EAWM. Furthermore, while previous studies mostly focused on the Holocene EAWM reconstructions, little attention has been paid to simulations of Holocene EAWM. It has been suggested that Northern Hemisphere ice sheets, input of glacial meltwater to the North Atlantic, and winter insolation can cause a change in the Holocene EAWM (Wang et al. 2008, 2012; Huang et al. 2011), but little work has been done on testing these hypotheses.

Eolian sediments from the dry lands of China have been used as an indicator to reconstruct the changes of the EAWM on orbital and millennial time scales (An and Porter 1997; Liu and Ding 1998; Lu et al. 2004; Yang et al. 2006, 2011). Recent studies indicated that loess in Central China not only was controlled by the EAWM, but was also influenced by the EASM, which controls the advance or retreat of the boundaries between the areas of desert and loess (Yang and Ding 2008). Eolian sediments at the southern edge of the Gobi Desert, western China, are less affected by the East Asian summer monsoon (EASM) due to an obstruction of the Qinghai–Tibet Plateau and are sensitive to winter monsoon changes (Fig. 1). The objective of the present paper is to develop a credible Holocene EAWM indicator at the southern edge of the Gobi Desert, Western China, and compare it with coupled climate model simulations, so as to explore the mechanisms of the Holocene EAWM. Two eolian sedimentary sections, at the southern edge of the Gobi Desert and the northern Qinghai–Tibet Plateau, were selected as an EAWM record in Western China (Fig. 1). Both bulk organic matter and pollen concentrates were used for the AMS ^{14}C dating and a comparison between them shows a reliable chronology. Proxy data, including grain-size, total organic carbon (TOC), magnetic susceptibility (MS) and carbonate content

(CC) were obtained from the two eolian sections. We compare our new EAWM indicator from the Gobi Desert with several coupled climate model simulations performed with the Community Climate System Model, version 3. One of these simulations was run in transient mode, incorporating all forcings hypothesized to impact the EAWM. The transient nature of this simulation makes possible a detailed comparison to EAWM evolution through the Holocene as inferred from proxy records. In addition, we analyze output from several equilibrium, "time-slice" experiments designed to more rigorously test the relative influences of insolation, Northern Hemisphere ice sheets, and North Atlantic meltwater forcing. Our findings will address the controlling factors and mechanisms of the Holocene EAWM.

2 Regional setting

The Gobi Desert, which measures over 1,600 km from southwest to northeast and 800 km from north to south, covers parts of northern and northwestern China and southern Mongolia (Fig. 1). The desert basins are bounded by the Altai Mountains and the grasslands and steppes of Mongolia on the north, and by the Hexi Corridor and Qinghai–Tibet Plateau to the southwest. The Gobi Desert is a cold desert, and located on a plateau roughly at 900–1,500 m above sea level (Zhao 1983, Fig. 1). The EAWM and Siberian high-pressure systems keep the Gobi Desert dry and very cold in winter. The average annual rainfall usually is less than 200 mm, while the EAWM can cause the Gobi Desert to reach temperature extremes of −40 °C in winter (Zhao 1983). The Gobi Desert is made up of several distinct ecological and geographic regions based on variations in climate and topography. Eolian sediments in the southern Gobi Desert are transported by the EAWM and the westerly winds, while a powerful jet stream can carry this dust across the northern Pacific (Gong et al. 2006). The sampling area of this study is located at the southern edge of the Gobi Desert, in the Northern Qilian Mountains and the Eastern Hexi Corridor. According to geographical divisions of China, the study area is located in the typical arid region of northwest China, where the modern climate is mainly controlled by the westerly winds and less affected by the EASM (Zhao 1983; Li et al. 2012a). On the southern side of the Qilian Mountains, the northeastern margin of the Qinghai–Tibetan Plateau can still benefit from the EASM water vapor transport, although the region does not belong to the typical monsoon region (Wang and Lin 2002; Li et al. 2012a). However, water vapor transported by the monsoon only rarely reaches the northern side of the Qilian Mountains (Li et al. 2012a).

The sampling site is at the upper reaches of the Shiyang River drainage area, which is roughly at geographical coordinates of 100°57′–104°57′E, 37°02′–39°17′N, while the length of the drainage path is about 300 km (Fig. 1). The Shiyang River drainage area can be divided into three climatic zones from south to north. (1) The alpine semi-arid area of the Qilian Mountains has an altitude of 2,000–5,000 m, annual rainfall of 300–600 mm, and annual evaporation of 700–1,200 mm. (2) The cool and arid central plains have an altitude of 1,500–2,000 m, annual rainfall of 150–300 mm, and annual evaporation of 1,300–2,000 mm. (3) The northern warm and dry area has an altitude of 1,300–1,500 m, annual rainfall less than 150 mm, and annual evaporation of 2,000–2,600 mm (Fig. 1, Chen and Qu 1992).

3 Materials, methods and simulations

3.1 Huangyanghe (a) and Huangyanghe (b) sections

Huangyanghe (a) (37°25′N 102°36′E, Altitude 2447 m, Depth 3.20 m) and Huangyanghe (b) (37°25′N 102°36′E, Altitude 2454 m, Depth 3.20 m) sections are located in Wuwei City, Gansu Province in Western China (Fig. 1). The two sections are 1 km apart and both situated on a terrace of the Haxi River, which is a tributary of the Shiyang River. On the northern foothills of the Qilian Mountains, the area is sensitive to EAWM and conducive to deposition of eolian sediments due to the blocking effect of the mountains, where the annual precipitation is ~500 mm and the average annual temperature is ~2 °C. The Huangyanghe (a) and Huangyanghe (b) sections were sampled at 2 cm interval, yielding 160 samples each for analysis of proxies. Figure 2 shows photos of the two sections.

3.2 Radiocarbon dating, grain-size, total organic carbon (TOC), magnetic susceptibility (MS) and carbonate content (CC)

Bulk organic matter and pollen concentrates were selected for AMS ^{14}C radiocarbon dating to establish chronologies for the Huangyanghe (a) and Huangyanghe (b) sections (Table 1). The AMS ^{14}C dates were measured at the Dating Laboratory of Peking University. Pollen concentrates as materials for AMS ^{14}C dating were extracted by treatment with acid and alkali, then sieving for enriching (Zhou et al. 1997; Li et al. 2012b). Dating samples of the pollen concentrates were checked under a microscope, then samples with large amounts of aquatic plant pollen and celluloses were excluded. Grain-size distribution of all samples was determined by the Malvern Mastersizer 2,000 particle analyzer that automatically yields the percentages of clay-, silt- and sand-size fractions, as well as median, mean and mode sample diameters. Total organic carbon (%TOC) was

Fig. 2 Photos of the Huang-
yanghe (a) and Huangyanghe
(b) eolian sedimentary sections
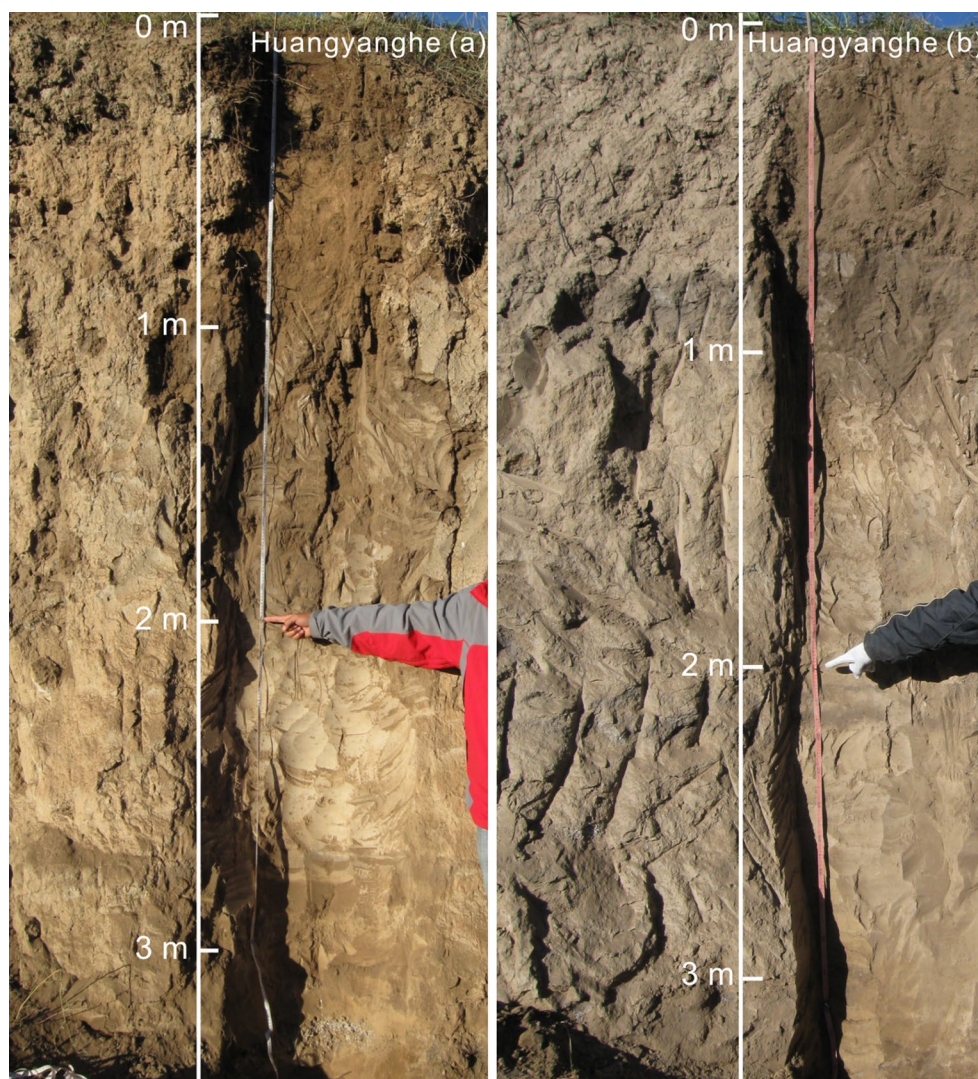
measured by Vario-III elemental analyzer; 5 g of sediment
was pretreated with 18 % HCl for 24 h at room tempera-
ture to remove inorganic carbonate. Magnetic susceptibil-
ity was measured using the Bartington MS2 magnetic sus-
ceptibility logger and carbonate content was measured by
SK-2T04 carbonate analyzer.

3.3 EAWM simulations

We analyzed equilibrium and transient simulations com-
pleted with the Community Climate System Model, version
3 (CCSM3). The CCSM3 consists of four component mod-
els of the ocean, sea ice, atmosphere and land that are cou-
pled without flux corrections. The transient experiment is
the TraCE (Transient Climate Evolution) experiment of the
last 21 ka, completed using the T31×3 resolution version
of this model (Liu et al. 2009b; He 2011). The atmospheric
model, Community Atmosphere Model version 3, thus
has a resolution of ~3.75 degrees in the horizontal and 26
vertical levels. The ocean model, an NCAR implementation
of the Parallel Ocean Program, has 25 vertical levels, a res-
olution of 3.6 degrees for longitude, and a variable resolu-
tion for latitude that is up to ~1 degree near the equator and
in the North Atlantic. We analyze the period from 13 ka
to present. Over this time period, the prescribed boundary
conditions and forcings are smooth orbitally-forced insola-
tion (Berger 1978) and atmospheric trace gas changes (Joos
and Spahni 2008), ice sheet extent and height updated
approximately every 500 years (Peltier 2004), coastline
changes made periodically (He 2011) and freshwater forc-
ing (Liu et al. 2009b; He 2011), as shown in Fig. 3. The
transient nature of this simulation enables continuous time
series comparison to proxy records and the ability to ana-
lyze rates of change through time.

We also analyze five equilibrium "time-slice" experi-
ments to both directly test the relative influence of orbital
forcing, ice sheets and meltwater forcing during the Early
Holocene and to verify the main outline of Holocene

Table 1 AMS ^{14}C ages for the Huangyanghe (a) and Huangyanghe (b) sections

Laboratory number	Depth (cm)	Dating materials	[14]C age (yr BP)	Calibrated ^{14}C age (2σ) (cal yr BP)
Huangyanghe (a)				
BA121247	100	Organic matter	1,165 ± 25	1,085 (988–1,172)
BA111241	152.5	Organic matter	1,970 ± 25	1,919 (1,873–1,988)
BA121244	176	Organic matter	3,395 ± 25	3,644 (3,576–3,696)
BA101282	202.5	Pollen concentrates	5,540 ± 25	6,337 (6,291–6,398)
BA121245	226	Organic matter	7,235 ± 35	8,048 (7,975–8,160)
BA121246	250	Organic matter	8,365 ± 40	9,397 (9,289–9,477)
BA101283	275	Pollen concentrates	10,780 ± 40	12,661 (12,570–12,791)
BA121243	300	Organic matter	9,820 ± 45	11,231 (11,179–11,307)
Huangyanghe (b)				
BA101276	67.5	Pollen concentrates	3,505 ± 25	3,773 (3,698–3,844)
BA121260	90	Organic matter	4,600 ± 35	5,322 (5,072–5,462)
BA121259	100	Organic matter	4,765 ± 25	5,522 (5,337–5,587)
BA111239	112.5	Organic matter	6,095 ± 30	6,963 (6,809–7,155)
BA121255	130	Organic matter	7,435 ± 35	8,263 (8,184–8,341)
BA121256	140	Organic matter	7,315 ± 30	8,109 (8,032–8,181)
BA121257	160	Organic matter	7,425 ± 30	8,260 (8,182–8,329)
BA121258	180	Organic matter	8,610 ± 30	9,552 (9,527–9,655)
BA121254	200	Organic matter	9,260 ± 35	10,443 (10,295–10,557)
BA111240	215	Organic matter	9,695 ± 40	11,144 (10,869–11,222)
BA121253	230	Organic matter	9,720 ± 35	11,176 (10,906–11,228)
BA101279	252.5	Pollen concentrates	9,785 ± 40	11,214 (11,167–11,254)
BA121252	260	Organic matter	9,875 ± 45	11,270 (11,207–11,391)
BA121248	270	Organic matter	10,310 ± 45	12,113 (11,849–12,385)
BA101280	292.5	Pollen concentrates	10,635 ± 35	12,591 (12,541–12,676)
BA121250	310	Organic matter	10,335 ± 35	12,170 (12,033–12,386)
BA121251	318	Organic matter	10,360 ± 40	12,222 (12,062–12,394)

climate evolution using a higher-resolution version of the model. The equilibrium simulations were completed at the T42×1 resolution of CCSM3 (Otto-Bliesner et al. 2006; Jin et al. 2012). The horizontal resolution of the atmosphere model is ~2.8º, and it has 26 vertical levels. The horizontal resolution of the ocean and sea ice models is nominally 1º with significantly greater resolution (up to 0.3 degrees) near the equator and in the North Atlantic. The ocean model has 40 vertical levels. Three of these simulations, for Pre-Industrial (ca. 1780 A.D.), 6, and 8.5 ka conditions, were forced only by orbital parameters. Two additional experiments for 8.5 ka include the effects of the remnant Laurentide Ice Sheet (8.5 ka ICE) and background meltwater fluxes entering the North Atlantic from the Hudson Strait (8.5 ka MELTICE) (Clarke et al. 2004, 2009). Boundary conditions and forcings were prescribed according to Table 2.

Figure 4 compares present-day winter circulation features simulated by the CCSM3 with the ERA-Interim reanalysis (Dee et al. 2011). Both the present-day control simulation as well as the present-day period of the TraCE simulation capture the large-scale circulation reasonably well, including the lower troposphere northwesterlies over the study region. The placement and strength of the Siberian High is likewise reasonable in the model. Additional details about model performance for simulations of paleoclimate and Asia are available in Otto-Bliesner et al. (2006) and Morrill et al. (2011).

Previous studies have applied different indices to measure the variability of EAWM from model simulations and meteorological observations (Yang et al. 2002; Jhun and Lee 2004; Hui 2007; Li and Yang 2010), including information about sea level pressure, meridional and/or zonal winds in the lower or upper troposphere, and geopotential height in the middle troposphere. In this study, we calculate two circulation indices for the EAWM: the 500 hPa geopotential height in the location of the monsoon trough over East Asia (Z500) and the strength of the polar jet stream at the 300 hPa level just south of Japan (U300). Jhun and Lee (2004) clearly explain how each of these circulation features relates to the larger
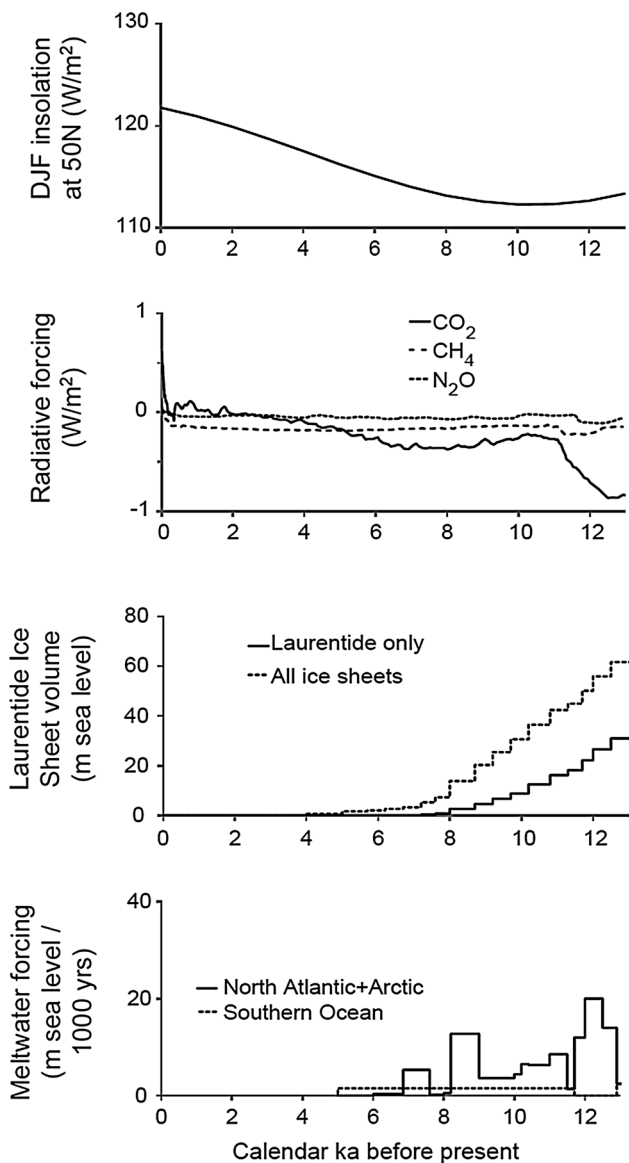
Fig. 3 Prescribed boundary conditions and forcings for the transient CCSM3 experiment (TraCE). (From *top* to *bottom*) Orbital parameters were set according to Berger (1978), radiative forcing from atmospheric greenhouse gases was from Joos and Spahni (2008), ice sheet area and height were set according to Peltier (2004), and meltwater forcing was set according to Liu et al. (2009b) and He (2011)

winter monsoon circulation. The canonical winter monsoon northwesterlies over northeastern Asia bring cold air from the polar region into East Asia, enhancing the meridional temperature gradient and, consequently, the core of the polar jet according to the thermal wind relationship. Anomalous cyclonic vorticity to the north of the polar jet enhances the monsoon trough at 500 hPa, which is associated with well-known winter "cold surges" during strong monsoon periods. We calculate Z500 and U300 as the normalized difference for winter (December–January–February) between two adjacent regions: 40–50°N, 130–170°E and 40–50°N, 60–100°E for Z500 and 25–35°N, 120–180°E and 55–65°N, 120–180°E for U300. The two regions for the Z500 calculation capture the locations of the monsoon trough and upstream ridge, while the U300 regions capture areas that typically have stronger (polar jet core) and weaker winds during a strong EAWM. This normalized difference approach is common in creating EAWM indices (e.g., Jhun and Lee 2004).

To further understand the reasons for changes in winter monsoon circulation, we consider the difference between the Siberian High and Aleutian Low pressure centers (ΔSLP). This pressure difference is key because the northwesterly monsoon winds over northeastern Asia are set up by the anticyclonic flow associated with the Siberian High and the cyclonic flow associated with the Aleutian low. We calculate ΔSLP as the normalized difference in winter (December–January–February) sea level pressure between 35–55°N, 80–100°E and 35–55°N, 150–170°W.

4 Results

4.1 Chronology

Table 1 shows the bulk organic matter and pollen concentrates AMS ^{14}C ages from the Huangyanghe (a) and Huangyanghe (b) sections and Fig. 5 indicates the relationship between ages and depths. There are 8 dates obtained from the Huangyanghe (a) section, two of which were dated by pollen concentrates. Seventeen dates were obtained from the Huangyanghe (b) section and three ages were measured by
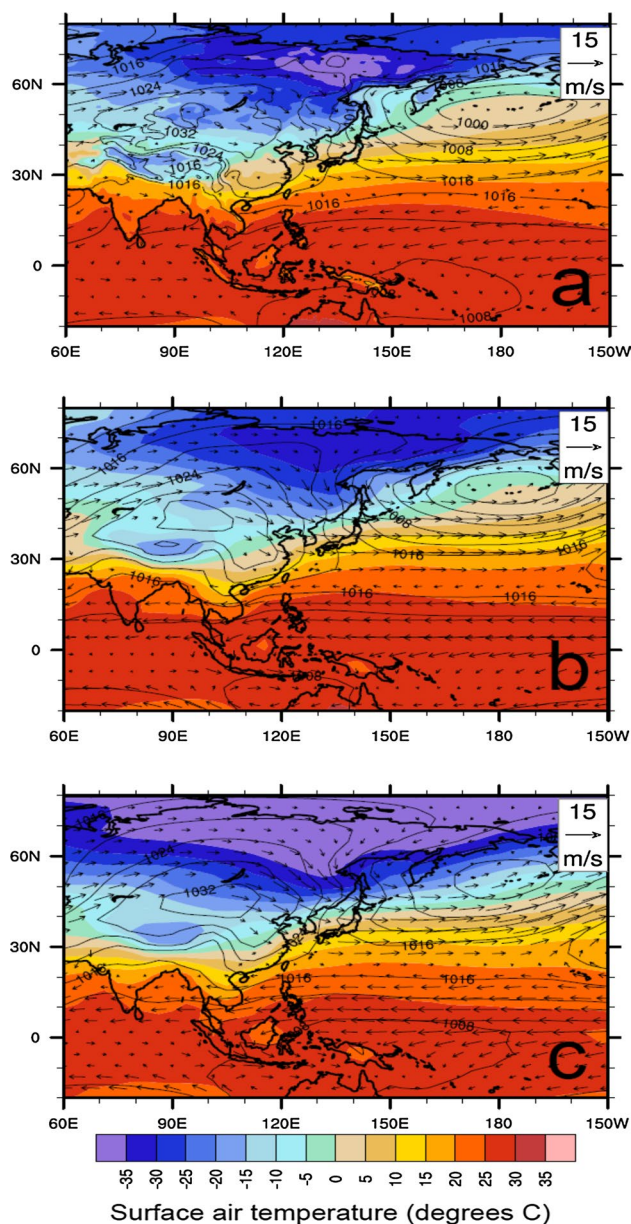
Table 2 Boundary conditions and forcings for CCSM3 equilibrium simulations

	PI	6 ka	8.5 ka	8.5 ka$_{ICE}$	8.5 ka$_{MELTICE}$
Eccentricity	0.016724	0.018682	0.019199	0.019199	0.019199
Obliquity (°)	23.45	24.10	24.22	24.22	24.22
Longitude of perihelion (°)	102.04	0.87	319.50	319.50	319.50
CO_2 (ppm)	280	280	260	260	260
CH_4 (ppb)	760	650	660	660	660
N_2O (ppb)	270	270	260	260	260
Laurentide ice sheet	None	None	None	Peltier (2004)	Peltier (2004)
St. Lawrence meltwater flux	None	None	None	None	0.05 Sverdrups

Fig. 4 Comparison of winter (December–January–February) surface temperature (°Celsius, colored contours), sea level pressure (hPa, *contour lines*), and 850 hPa winds (m/s, vectors) for (**a**) ERA Interim Reanalysis for 1979–2012 A.D. (Dee et al. 2011), (**b**) CCSM3 present-day control simulation for 1990 A.D., and (**c**) CCSM3 TraCE transient simulation for 1950–1980 A.D

in the two sections. For example, a radiocarbon age from pollen concentrates at 202.5 cm of the Huangyanghe (a) section is $5,540 \pm 25$ [14]C yr BP, while two bulk organic matter ages at 176 and 226 cm are $3,395 \pm 25$ [14]C yr BP and $7,235 \pm 35$ [14]C yr BP, respectively. Another radiocarbon age from pollen concentrates at 252.5 cm of the Huangyanghe (b) section is $9,785 \pm 40$ [14]C yr BP, which is also consistent with the ages from above and below layers. Therefore, according to a comparison between different dating materials, the chronologies of the two sections are generally reliable and the carbon reservoir effect is relatively slight. With regard to the purpose of this study, the dating error will not affect the long-term reconstruction of Holocene EAWM. It is noted that there are two ages from pollen concentrates that are slightly older than ages from the upper layers [275 cm, $10,780 \pm 40$ [14]C yr BP at the Huangyanghe (a) section; 292.5 cm, $10,635 \pm 35$[14]C yr BP at the Huangyanghe (b) section]. Pollen is small in size and light in weight, which is easily transported by wind. Eolian sediments, as well as pollen and spores, can be transported by wind from large areas in East and Central Asia; therefore, some old pollen is easily transported to the site. Bulk organic matter ages are less likely to be affected by the old pollen because of the small amount. Radiocarbon ages (^{14}C yr BP) were calibrated to calendar years (Cal yr BP) using the software of Calib6.11. Quantitative relationships between calibrated ages and depths were established according to a liner fitting ($R^2 = 0.9318$) at the Huangyanghe (a) section and a quadratic curve fitting ($R^2 = 0.9828$) at the Huangyanghe (b) section (Fig. 5).

4.2 Grain-size, total organic carbon (TOC), magnetic susceptibility (MS) and carbonate content

The average median, mean and mode grain-size are 18.76, 35.75 and 33.91 μm at the Huangyanghe (a) section and 21.77, 38.22 and 32.33 μm at the Huangyanghe (b) section. The overall grain-size is similar for the two sections (Fig. 6). Figure 7 shows the average grain-size frequency curves for the two sections, which are similar to each other and indicating that the peaks of grain-size frequency distribution are at 28 μm for the Huangyanghe (a) section and 32 μm for the Huangyanghe (b) section. The average clay, silt and sand contents are 15.32, 73.51 and 11.17 % at the Huangyanghe (a) section and 13.09, 73.59 and 13.32 % at the Huangyanghe (b) section (Fig. 6). Grain-size components are also similar for them, and silt is a major component for the two sections. Figure 6 shows variability of median, mean and mode grain-size, as well as clay, silt and sand contents from the two sections. There is an obvious shift in mode grain size at ~183 cm (5,088 cal yr BP) of the Huangyanghe (a) section, while the same condition can also be found at the Huangyanghe (b) section (Fig. 6). The
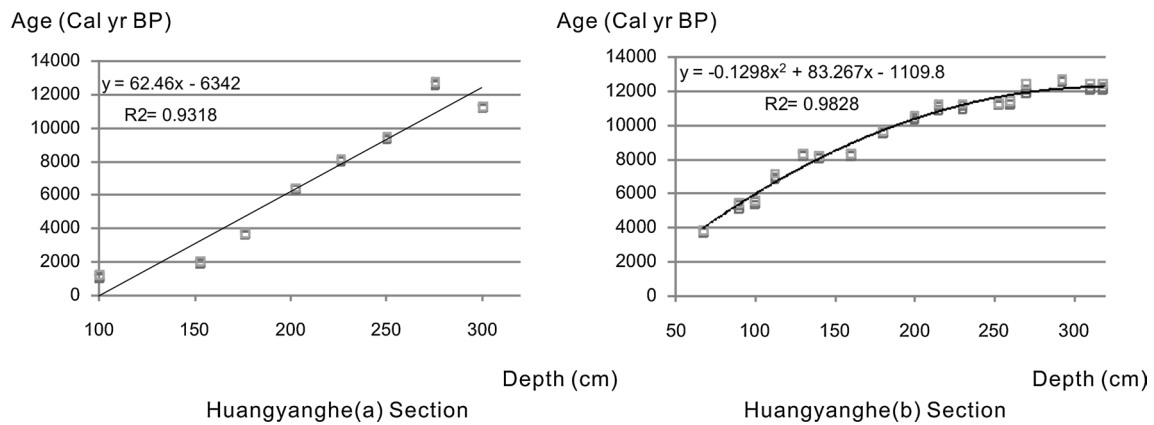
pollen concentrates. Based on the twenty-five radiocarbon ages, it can be seen that the two sections were well dated and mostly formed during the Holocene. Compared with lacustrine sediments, the carbon reservoir effect is relatively weak in eolian sediments due to a low carbon exchange rate. Terrestrial pollen concentrates are ideal dating materials to evaluate the carbon reservoir effect in eolian sediments (Zhou et al. 1997). The five pollen concentrates radiocarbon dates are relatively consistent with bulk organic matter ages

Fig. 5 Correlation between calibrated ^{14}C ages and depths for the Huangyanghe (a) and Huangyanghe (b) sections. *Error bars* for the calibrated ^{14}C ages were also shown in this figure
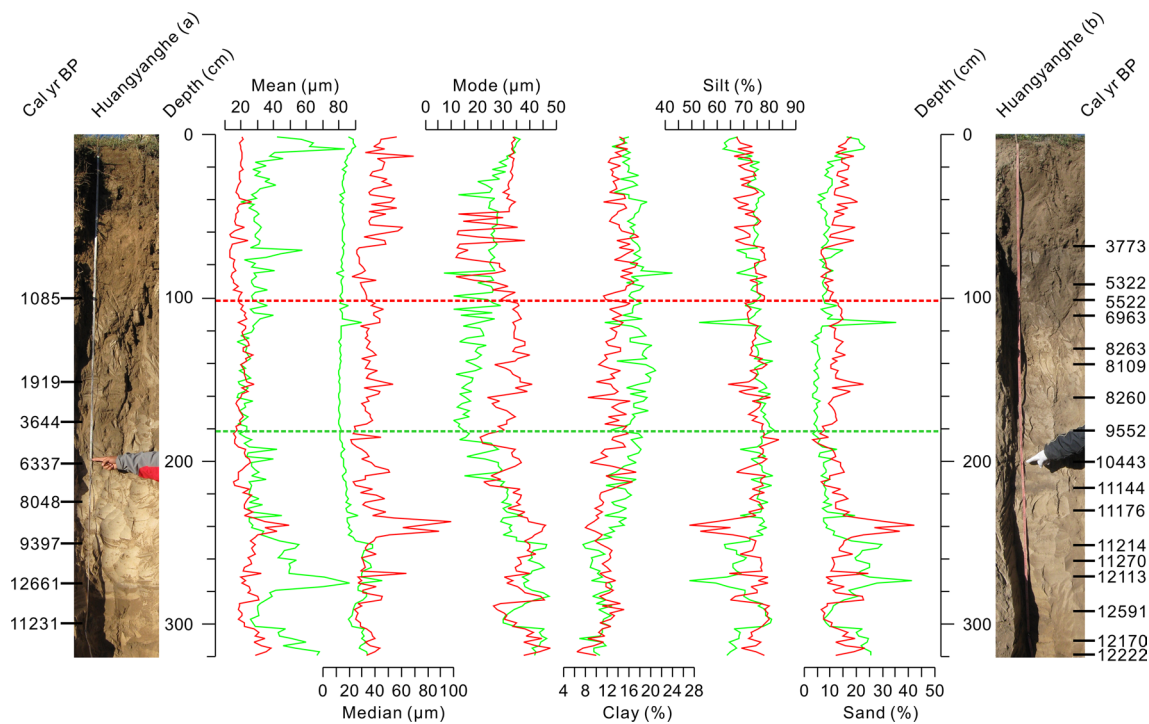

Fig. 6 Lithology, grain-size and calibrated ^{14}C ages for the Huang-yanghe (a) and Huangyanghe (b) sections. *Green curves* are from the Huangyanghe (a) section while *red curves* are from the the Huang-yanghe (b) section. The *green dashed line* indicates the obvious mode grain size shift at the Huangyanghe (a) section; the *red one* indicates the mode grain size shift at the Huangyanghe (b) section

thinning trend in grain-size is clear at the Huangyanghe (b) section based on variability of clay contents, median and mode grain-size. Below ~103 cm (~6,089 cal yr BP), grain-size is relatively coarse at the Huangyanghe (b) section, while the average median, mean and mode grain-size are 23.85, 39.23 and 34.18 μm, compared with 17.80, 39.76 and 27.50 μm for the upper part. The average clay content is increased from 12.42 % in the lower part to 14.53 % in the upper part. There is a thinning trend

in grain-size from early to late Holocene for the two sections, which can be detected although affected by several steps and peaks. Furthermore, there is an obvious turning point in the middle Holocene (~6.0–~5.0 cal kyr BP). The depositional environment is different below or above the turning point, showing a change in the eolian depositional system.

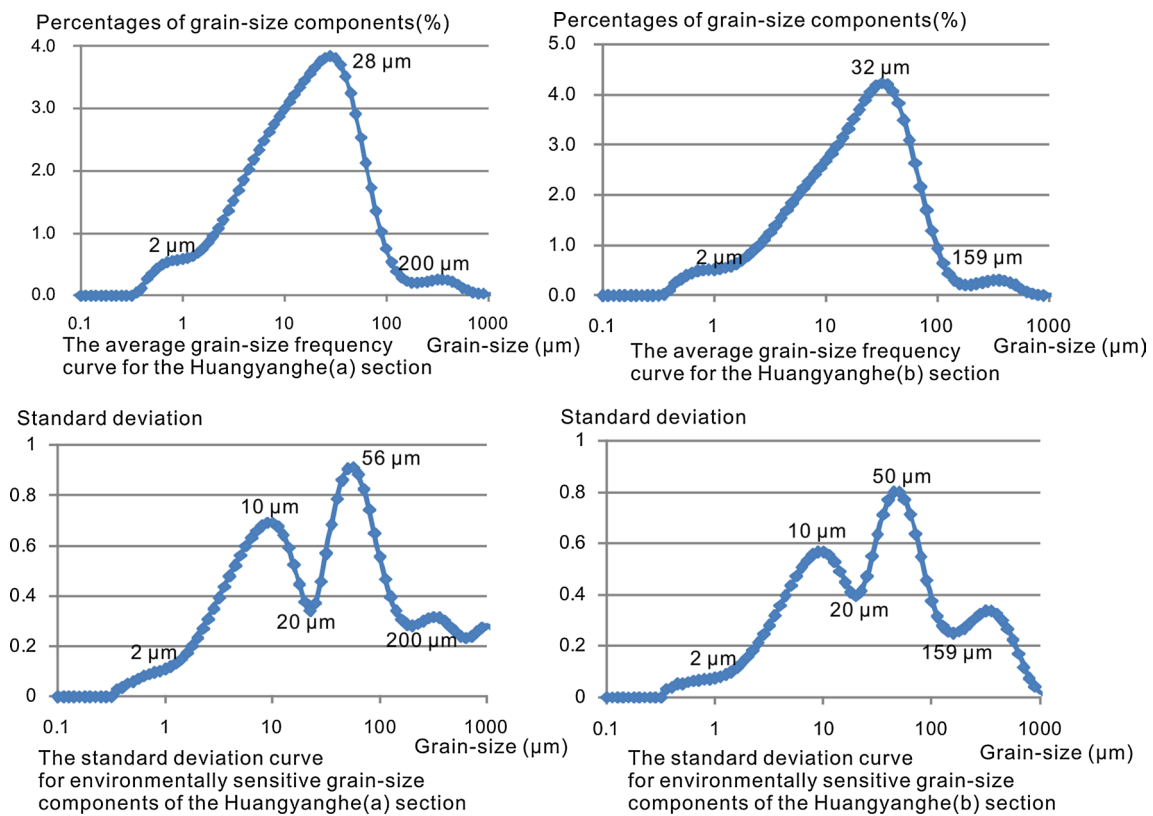As has been shown in Fig. 8, changing trends of proxy data, including total organic carbon (TOC %), magnetic

Fig. 7 The average grain-size frequency distribution curves and the grain-size standard deviation curves from the Huangyanghe (a) and Huangyanghe (b) sections

susceptibility (MS $\chi/10^{-8}$ m^3 kg^{-1}) and carbonate content (CC %), are relatively consistent with changes in grain-size. The average TOC, MS and CC are 1.51 %, 86.25 and 4.46 % for the Huangyanghe (a) section, and 1.14 %, 73.47 and 5.87 % for the Huangyanghe (b) section. There is a clear increasing trend for TOC and MS of the two sections from early to late Holocene, while the CC indicates a decreasing trend from bottom to top, but an abrupt increase of CC appears at the top of the Huangyanghe (a) section, which may be related to modern human impacts. The increasing trend for TOC and MS and the decreasing trend in CC correspond to the thinning tendency in grain-size from the early to late Holocene. At the Huangyanghe (a) section, the average TOC, MS and CC are 0.79 %, 50.91 and 4.83 % below ~183 cm (5,088 cal yr BP), while the upper ones are 2.05 %, 112.37 and 4.18 %. Below ~103 cm (~6,089 cal yr BP), the average TOC, MS and CC are 0.69 %, 45.18 and 7.34 % at the Huangyanghe (b) section, which are 2.09 %, 132.23, 2.84 % for the upper part (Fig. 8).

4.3 EAWM indicators

Grain-size data have been widely used to reconstruct eolian depositional environment, which is closely related to the EAWM in Northern China, and significant scientific achievements have been made on a long time scale (An et al. 1991; Xiao et al. 1995; An and Porter 1997; Lu et al. 2004). Environmentally sensitive grain-size components, extracted from grain-size data, can be used to show variability of various climatic factors, such as winter monsoon and effective moisture (Prins et al. 2000; Sun et al. 2002; Xiao et al. 2005). In this study, we used the grain-size standard deviation model to extract environmentally sensitive grain-size components from the grain-size frequency distribution curve (Xiao et al. 2005; Hu et al. 2012). The method is to calculate the standard deviation of frequency distribution data for all samples then determining the sensitivity of every grain-size component. Standard deviation is a measure of central tendency (how spread out your data is) from the average, which is always used with the average and not with the mode. A large standard deviation means your data is very spread out, a small one means your data is grouped closely together. Please see a more detailed description in Xiao et al. (2005) and Hu et al. (2012).

Figure 7 shows curves of the grain-size standard deviation model for the two sections, and there are four environmentally-sensitive grain-size components for each section: <2, 2–20, 20–200 and >200 μm from the Huangyanghe
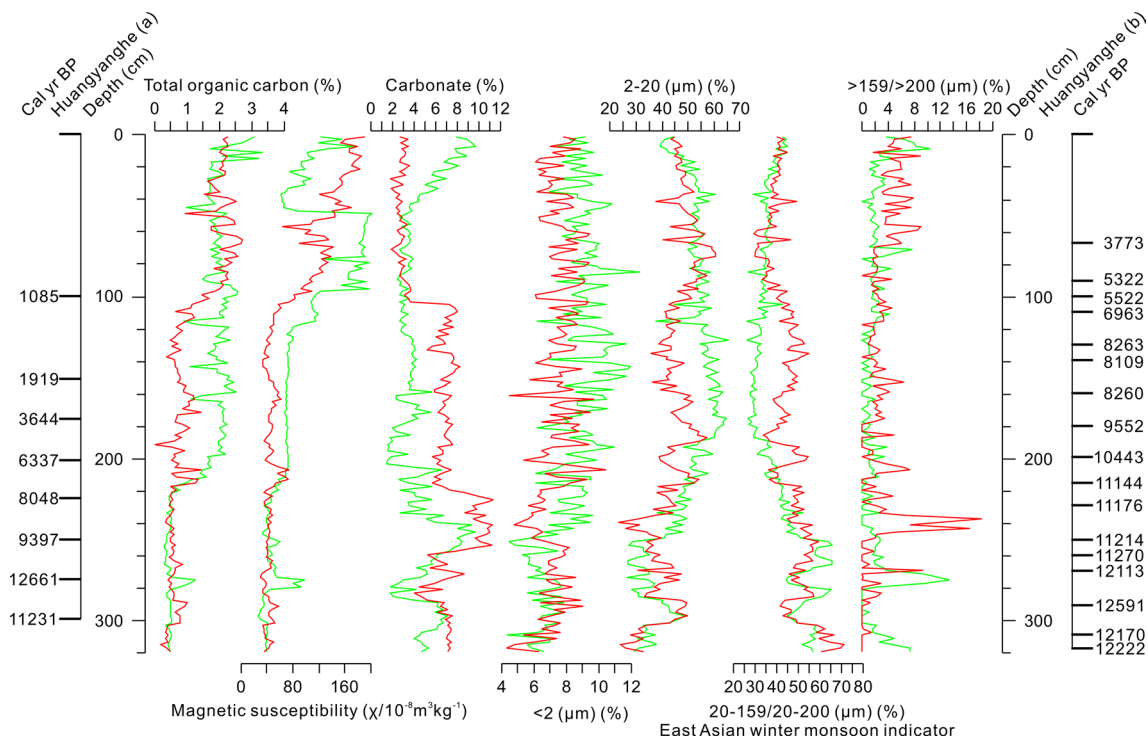
Fig. 8 Total organic carbon, magnetic susceptibility, carbonate content and environmentally sensitive grain-size components extracted based on the standard deviation model for the Huangyanghe (a) and Huangyanghe (b) sections. *Green curves* are from the Huangyanghe (a) section while red curves are from the the Huangyanghe (b) section

(a) section and <2, 2–20, 20–159 and >159 μm from the Huangyanghe (b) section. The extreme fine-grained or clay fraction (<2 μm), extracted from the two sections, has been widely reported in northern China. Investigations on eolian particle dynamics have found that the coarse particles, or silt fraction in aeolian sediments, are generally transported by surface winds and moves (Sun et al. 2002; Pye 1995). The fine-grained particles or clay fraction can be dispersed within a wide altitudinal extent and are mainly transported by upper level air flow; however, the upper level air flow is less related to the winter monsoon compared with surface winds (Pye 1995; Rea et al. 1985). Therefore, the extreme fine-grained fraction is not usually used as a proxy of the EAWM (Pye 1995; Rea et al. 1985; Sun et al. 2002, 2008). The extremely coarse components, >200 μm at the Huangyanghe (a) section and >159 μm at the Huangyanghe (b) section, are usually related to severe duststorm events that are not directly correlated with the EAWM (Sun et al. 2002, 2008). As a result, we can choose the EAWM indictor from 2–20 and 20–200 μm at the Huangyanghe (a) section and 2–20 and 20–159 μm at the Huangyanghe (b) section. Grain-size data from eolian sediments in northern China are generally composed of a coarse component and a finer overlapping component, which are similar to the two remaining components in this study (Sun et al. 2004). Studies of modern dusts and variations of the two grain-size

components suggest that the coarse component was transported mainly by low-altitude northwesterly winds of the EAWM circulation (Sun et al. 2004; Weltje and Prins 2007), while the finer part probably comes from the high-altitude westerly air flow. Therefore, the coarser components from the two sections, 20–200 μm at the Huangyanghe (a) section and 20–159 μm at the Huangyanghe (b), were chosen as the EAWM indicator. Figure 8 indicates changes of the four environmentally-sensitive grain-size components from the two sections.

Total organic carbon (TOC) of eolian sediments can also be related to the EAWM in northern China, since a strong winter monsoon will reduce the next year's plant growth and is not conducive to preservation of organic matter (Xiao et al. 2002), while magnetic susceptibility (MS) has been used as an millennial-scale EAWM indicator (Fang et al. 1999). Carbonate content (CC) is directly affected by carbonate leaching processes that may also be influenced by the EAWM on the long-term time scales (He et al. 2013). A comparison of the EAWM indicator [20–200 μm at the Huangyanghe (a) section and 20–159 μm at the Huangyanghe (b)], TOC, MS and CC from the two sections has been shown in Figs. 8 and 9. The EAWM indicator is negatively correlated with TOC and MS, and positively correlated with CC, showing that when the EAWM is strong the TOC and MS values are relatively low and the CC values
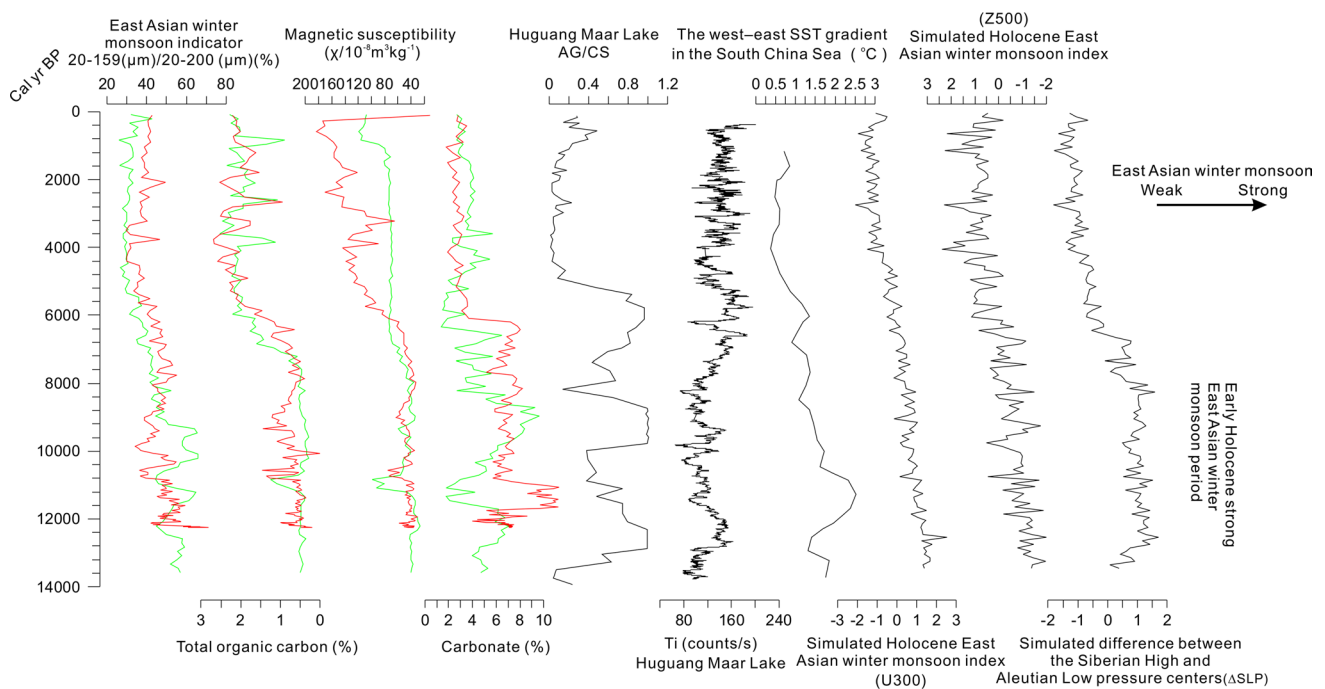
Fig. 9 A comparison of the simulated Holocene EAWM indices as described in text: the 500 hPa geopotential height in the location of the monsoon trough over East Asia (Z500) and the strength of the polar jet stream at the 300 hPa level just south of Japan (U300); the simulated difference between the Siberian High and Aleutian Low pressure centers (ΔSLP); the EAWM indicator [the 20–200 μm component for the Huangyanghe (a) section and the 20–159 μm component for the Huangyanghe (b) section] and proxy data of total organic carbon, magnetic susceptibility, carbonate content for the Huangyanghe (a) and Huangyanghe (b) sections and previous Holo- cene East Asian winter monsoon reconstructions including AG/CS (the ratio between A. granulata and C. stelligera) from Huguang Maar Lake (Wang et al. 2012), Ti (counts/s) from Huguang Maar Lake (Yancheva et al. 2007), the west–east SST gradient (°C) between the southwestern and southeastern SST stacks in the South China Sea (Huang et al. 2011). Green curves are from the Huangyanghe (a) sec- tion while *red curves* are from the the Huangyanghe (b) section. All of the simulated data are standardized in the figure. All time series have been oriented such that stronger winter monsoon conditions are to the right

are relatively high, and vice versa. This is consistent with our understanding of these proxies (Fang et al. 1999; Xiao et al. 2002; He et al. 2013). During the Last Deglaciation and early Holocene, the EAWM is relatively strong and there is a turning point in the middle Holocene (~7.0–~6.0 cal kyr BP) for the evolution of the Holocene EAWM; after that, the EAWM is weakened. An abrupt EAWM fluctuation was found between ~12.0 and ~10.5 cal kyr BP, which can be related to the Younger Dryas (YD) event showing impacts of the extreme cold event to the EAWM.

4.4 EAWM simulations

Figure 9 shows a comparison between the reconstructed Holocene EAWM variability and the simulated Holocene EAWM indices. They indicate a consistent changing trend, a strong early Holocene EAWM and a generally smooth weakening tendency. As mentioned above, the proxies show a steeper trend in the mid Holocene ca. 6 ka. This does appear in some of the model time series from the TraCE experiment, most notably in the ΔSLP.

The equilibrium simulations also generally show a weakening pattern through the Holocene, particularly when comparing simulations with only orbital forcing. In fact, the early Holocene equilibrium simulations indicate that the addition of a remnant Laurentide Ice Sheet and back- ground meltwater flux weaken the winter monsoon com- pared to the orbital-only simulation. From this, we can conclude that the relatively stronger winter monsoon in the early Holocene compared to the late Holocene is due to orbital forcing.

The SLP can further explain the trends in the winter monsoon circulation patterns described by the Z500 and U300 indices (Fig. 9). Therefore, it is important to under- stand what drives changes in the sea level pressure differ- ence. Figure 10 shows surface temperature and sea level pressure anomaly maps for the different simulations. It is clear that for the middle and early Holocene, orbital forcing causes an enhanced land-sea temperature contrast in win- ter. This enhances the sea level pressure difference between the Siberian High and the Aleutian Low, mostly through deepening the Aleutian Low. Similar increased land-sea
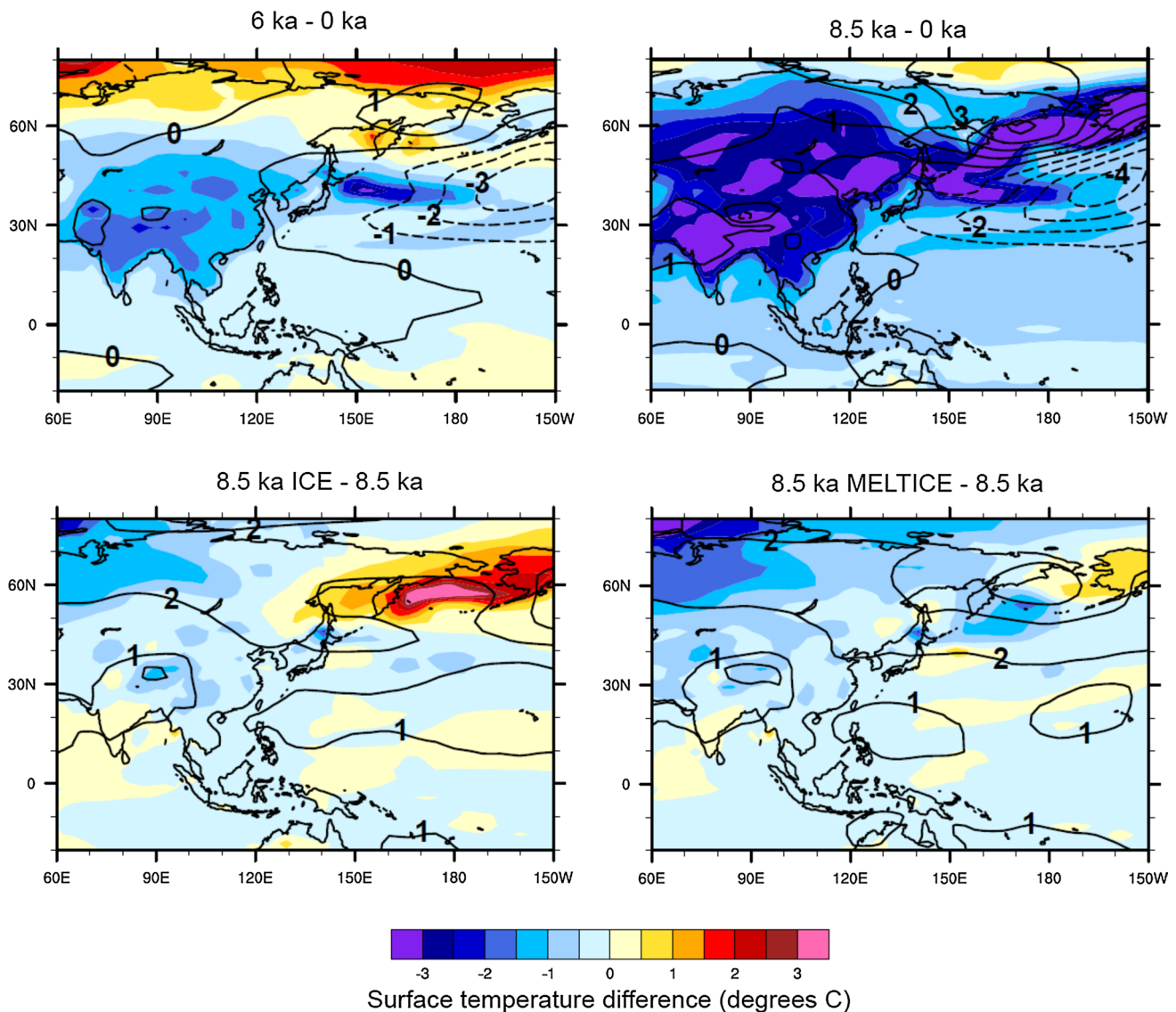
Fig. 10 Differences in winter (December–January–February) surface temperature (°Celsius, colored contours) and sea level pressure (hPa, contour lines) between the CCSM3 equilibrium simulations. Negative contour lines are *dashed*

temperature contrast is not observed due to adding the Laurentide ice sheet or the background meltwater flux down the St. Lawrence River.

5 Discussion

5.1 Comparison with previous studies

In this study, we reconstructed the Holocene EAWM history on the basis of 25 AMS ^{14}C dates, the grain-size standard deviation model and proxy data from two sedimentary sections at the southern edge of the Gobi Desert, which shows a strong early Holocene EAWM and a

declining trend since the middle Holocene (~6.0–~5.0 cal kyr BP). For the general changing trend, the calculated Holocene EAWM circulation patterns using a transient simulation and several equilibrium experiments agrees with the reconstructed winter monsoon intensity. Our new Holocene EAWM record has some similarities and some differences with previous work. For example, Wang et al. (2008, 2012) used high-resolution diatom assemblages as a proxy indicator of the EAWM from Huguang Maar Lake and their results showed that the EAWM shifted from strong to weak from the early to late Holocene (Fig. 9). An enhanced EAWM during the early Holocene is also shown by the reconstructed Holocene west–east SST gradient from the South China Sea (Huang et al. 2011) (Fig. 9).

Environmentally-sensitive grain-size data from the Central Yellow Sea, Eastern China also indicate that the evolutionary history of the EAWM broadly follows the orbitally-derived winter insolation with a similar Holocene long-term decreasing trend as the EASM (Hu et al. 2012). On the contrary, the high-resolution record of titanium concentration from the Huguang Maar Lake in subtropical China indicates that the EAWM was strengthened from the early Holocene to late Holocene (Yancheva et al. 2007) (Fig. 9). In Central China, Yang and Ding (2008) found that the grain-size of many loess records shows a consistent result with the result from Yancheva et al. (2007). Our results of the Holocene EAWM are generally supported by multidisciplinary data from lacustrine and marine sediments (Wang et al. 2008, 2012; Tian et al. 2010; Huang et al. 2011; Hu et al. 2012) (Fig. 9). The reliability of the MS, S-ratio and Ti content records from the Huguang Maar Lake as indicators of the EAWM has also been questioned due to the provenance of the sediments (Zhou et al. 2009; Han et al. 2010). In addition, loess records in Central China are not only controlled by the EAWM, but also influenced by the EASM that affects boundary changes of the desert and loess areas (Yang and Ding 2008). As a result, there can be some misunderstandings regarding the records that indicate strengthened EAWM from the early Holocene to late Holocene. This study further confirms a strong early Holocene EAWM and a declining trend since the middle Holocene.

Furthermore, the relationship between Holocene EAWM and EASM is another focus of research. In the South China Sea, a ΔSST record shows that after ~8.5 kyr the EAWM strengthened relative to the last Deglaciation, similar to the strengthening of the EASM, while Holocene summer and winter monsoon strength probably are not anti-correlated (Tian et al. 2010). In the Northern Qinghai–Tibetan Plateau, a late Holocene record from Kusai Lake suggests that intensified winter and summer monsoons are well correlated with respective reductions and increases in solar irradiance (Liu et al. 2009a). In the Eastern Qinghai–Tibet Plateau, a peat sequence from the Hongyuan Swamp using the dust flux and the content of trace metallic elements shows different patterns of changes in the Asian winter and summer monsoons before and after 5.5 cal ka BP (Yu et al. 2011). During the early Holocene, the EASM was strengthened by the increased low-latitude solar insolation in the Northern Hemisphere, which has been widely confirmed by paleoclimate records in the typical monsoon domain; and then, the intensity of EASM circulation declined in response to changes in insolation and a southward shift in the ITCZ (Fleitmann et al. 2003; Dykoski et al. 2005; Morrill et al. 2006; Cai et al. 2010). Our new record shows that the evolution pattern of Holocene EAWM at the southern edge of the Gobi Desert is consistent with EASM reconstructions from the Asian summer monsoon domain.

However, abrupt climatic events on the centennial or decadal-scale may have different impacts to EAWM and EASM (Hu et al. 2012). Moreover, the winter and summer monsoon systems may have different responses on even longer time scales, for example glacial-interglacial cycles (Sun et al. 2012; Huang et al. 2011). It is important to pay more attention to time scales when explaining the EAWM records and understanding the relationship between winter and summer monsoon.

5.2 Mechanisms of the Holocene EAWM evolution

Our results show that both the EASM and the EAWM display a similar long-term decreasing trend since the early Holocene, resulting from the orbital forcing seasonal variation of solar insolation in the Northern Hemisphere (Berger and Loutre 1991). A similar conclusion was reached in a previous study comparing equilibrium simulations for 6 and 0 ka (Zhou and Zhao 2009). That study also identified the importance of the land-sea temperature contrast in affecting the ΔSLP. Our result is somewhat different from that of Shi et al. (2011), who concluded that the EAWM is driven primarily by obliquity forcing and its effects on the meridional temperature gradient rather than the zonal gradients we identify. Part of this inconsistency could be due to the fact that those authors considered only the strength of the Siberian High, rather than the zonal ΔSLP, in understanding EAWM variations. Even though the ΔSLP appears to do a good job in explaining the Z500 and U300 indices for the EAWM in our simulations, it is possible that meridional temperature differences forced by obliquity could make an additional contribution.

An important conclusion from our study is that other candidates for causing a strong EAWM during the early Holocene, the remnant Laurentide ice sheet and the background freshwater forcing, were not significant. Both of these forcings seemed like plausible causal factors based on previous work. It has been hypothesized, for example, that large Northern Hemisphere ice sheets were responsible for the strong EAWM during glacial periods (e.g., Liu and Ding 1993; Ding et al. 1995). Also, meltwater forcing during Heinrich events of the last glacial period has been shown to cause significant strengthening of the EAWM in model simulations (e.g., Sun et al. 2012). Both the Laurentide ice sheet and North Atlantic meltwater forcings were significantly smaller during the early Holocene than they were during glacial times, however (only ~5 % of full glacial values).

Our findings are consistent with future projections of EAWM from coupled climate models. Generally, models indicate that the EAWM will become weaker in the future due to increased concentrations of atmospheric greenhouse gases (Hori and Ueda 2006; Jiang and Tian 2012). The weakening

of the winter monsoon in these models appears tied to a reduction of the ΔSLP as both the Siberian High and Aleutian Low weaken. One likely cause of reduced ΔSLP is greater heating of the land surface than the ocean surface by the greenhouse gas forcing (Hu et al. 2000; Jiang and Tian 2012).

6 Conclusions

A Holocene eolian EAWM record was collected at the southern edge of the Gobi Desert, while twenty-five AMS ^{14}C ages and proxy data were obtained. Holocene EAWM history was reconstructed using environmentally-sensitive grain-size components, which were extracted by the grain-size standard deviation model and were consistent with total organic matter, magnetic susceptibility and carbonate content data. The results show a strong early Holocene EAWM and a turning point for the changes during the middle Holocene, after that the intensity of the EAWM declines gradually. Based on output from transient and equilibrium simulations using the CCSM3, we analyzed changes in EAWM during the Holocene. The results indicate a gradually decreasing trend since the early Holocene, which agrees with our reconstructed Holocene EAWM intensity. The model results also show a broad agreement with other lacustrine and marine EAWM records in Eastern and Southern China. The transient model simulated significantly decreased EAWM at the mid-to-late Holocene in East Asia compared to the early Holocene. Orbital forcing, which increased the land–ocean temperature and sea level pressure contrast, can explain this trend. Other forcings, including the remnant Laurentide ice sheet and meltwater forcing in the North Atlantic, were too small to explain the strong EAWM during the early Holocene. This study generally confirms that the relationship between winter and summer monsoon is different on various time scales, and supports the proposed mechanisms for future winter monsoon changes in East Asia.

References

An ZS, Porter SC (1997) Millennial-scale climatic oscillations during the last interglaciation in central China. Geology 25:603–606

An ZS, Kukla G, Porter SC, Xiao JL (1991) Late Quaternary dust flow on the Chinese loess plateau. Catena 18:125–132

Berger AL (1978) Long-term variations of caloric insolation resulting from the Earth's orbital elements. Quat Res 9:139–167

Berger AL, Loutre MF (1991) Insolation values for the climate of the last 10,000,000 years. Quat Sci Rev 10:297–317

Cai Y, Tan L, Cheng H, An Z, Edwards RL, Kelly MJ, Kong X, Wang X (2010) The variation of summer monsoon precipitation in central China since the last deglaciation. Earth Planet Sci Lett 291:21–31

Chang CP, Lau KM (1980) Northeasterly cold surges and near-equatorial disturbances over the winter MONEX area during December 1974. Part II: planetary-scale aspects. Mon Weather Rev 108:298–312

Chang CP, Lau KM (1982) Short-term planetary-scale interaction over the tropics and midlatitudes during northern winter. Part I: contrasts between active and inactive periods. Mon Weather Rev 110:933–946

Chen L, Qu Y (1992) Water–land resources and reasonable development and utilization in the Hexi region. Science Press, Beijing (in Chinese)

Clarke GKC, Leverington DW, Teller JT, Dyke AS (2004) Paleohydraulics of the last outburst flood from glacial Lake Agassiz and the 8200 BP cold event. Quat Sci Rev 23:389–407

Clarke GKC, Bush ABG, Bush JWM (2009) Freshwater discharge, sediment transport, and modeled climate impacts of the final drainage of Glacial Lake Agassiz. J Clim 22:2161–2180

Compo GP, Kiladis GN, Webster PJ (1999) The horizontal and vertical structure of east Asian winter monsoon pressure surges. Q J R Meteorol Soc 125:29–54

Dee DP, Uppala SM, Simmons AJ, Berrisford P, Poli P, Kobayashi S, Andrae U, Balmaseda MA, Balsamo G, Bauer P, Bechtold P, Beljaars ACM, van de Berg L, Bidlot J, Bormann N, Delsol C, Dragani R, Fuentes M, Geer AJ, Haimberger L, Healy SB, Hersbach H, Holm EV, Isaksen L, Kallberg P, Kohler M, Matricardi M, McNally AP, Monge-Sanz BM, Morcrette JJ, Park BK, Peubey C, de Rosnay P, Tavolato C, Thepaut JN, Vitart F (2011) The ERA-Interim reanalysis: configuration and performance of the data assimilation system. Q J R Meteorol Soc 137:553–597

Ding YH (1990) Build-up, air mass transformation and propagation of Siberian high and its relation to cold surge in east Asia. Meteorol Atmos Phys 44:281–292

Ding YH, Krishnamurti TN (1987) Heat budget of Siberian high and winter monsoon. Mon Weather Rev 115:2428–2449

Ding Z, Liu T, Rutter NW, Yu Z, Guo Z, Zhu R (1995) Ice-volume forcing of east Asian winter monsoon variations in the past 800,000 years. Quat Res 44:149–159

Dykoski CA, Edwards RL, Cheng H, Yuan D, Cai Y, Zhang M, Lin Y, Qin J, An Z, Revenaugh J (2005) A high-resolution, absolute-dated Holocene and deglacial Asian monsoon record from Dongge Cave, China. Earth Planet Sci Lett 233:71–86

Fang XM, Ono Y, Fukusawa H, Pan B, Li JJ, Guan D, Oi K, Tsukamoto S, Torii M, Mishima T (1999) Asian summer monsoon instability during the past 60,000 years: magnetic susceptibility and pedogenic evidence from the western Chinese Loess Plateau. Earth Planet Sci Lett 168:219–232

Fleitmann D, Burns SJ, Mudelsee M, Neff U, Kramers J, Mangini A, Matter A (2003) Holocene forcing of the Indian monsoon recorded in a stalagmite from Southern Oman. Science 300:1737–1739

Gong DY, Ho CH (2003) Arctic oscillation signals in the East Asian summer monsoon. J Geophys Res 108(D2):4066. doi:10.1029/2002JD002193

Gong DY, Wang SW, Zhu JH (2001) East Asian winter monsoon and Arctic oscillation. Geophys Res Lett 28:2073–2076

Gong SL, Zhang XY, Zhao TL, Zhang XB, Barrie LA, McKendry IG, Zhao CS (2006) A simulated climatology of Asian dust aerosol and its trans-Pacific transport 2.Interannual variability and climate connections. J Clim 19:104–122

Han Y, Tan X, Chen Z, Xiang R, Zhang L (2010) Magnetic granulometry of recent sediments from the Huguang Maar and its implication for provenience. Chin Sci Bull 55:418–424

He F (2011) Simulating transient climate evolution of the last deglaciation with CCSM3. Department of Atmospheric and Oceanic Sciences, University of Wisconsin, Madison, p 171

He T, Chen Y, Balsam W, Qiang X, Liu L, Chen J, Ji J (2013) Carbonate leaching processes in the Red Clay Formation, Chinese Loess Plateau: Fingerprinting East Asian summer monsoon variability during the late Miocene and Pliocene. Geophys Res Lett doi:10.1029/2012GL053786

Hori ME, Ueda H (2006) Impact of global warming on the East Asian winter monsoon as revealed by nine coupled atmosphere-ocean GCMs. Geophys Res Lett 33:L03713

Hu ZZ, Bengtsson L, Arpe K (2000) Impact of global warming on the Asian winter monsoon in a coupled GCM. J Geophys Res 105:4607–4624

Hu B, Yang Z, Zhao M, Saito Y, Fan D, Wang L (2012) Grain size records reveal variability of the East Asian Winter Monsoon since the Middle Holocene in the Central Yellow Sea mud area, China. Sci China Earth Sci 55:1656–1668

Huang E, Tian J, Steinke S (2011) Millennial-scale dynamics of the winter cold tongue in the southern South China Sea over the past 26 ka and the East Asian winter monsoon. Quat Res 75:196–204

Hui G (2007) Comparison of East Asian winter monsoon indices. Adv Geosci 10:31–37

Jhun JG, Lee EJ (2004) A new East Asian winter monsoon index and associated characteristics of the winter monsoon. J Clim 17:711–726

Jiang DB, Tian ZP (2012) East Asian monsoon change for the 21st century: results of CMIP3 and CMIP5 models. Chin Sci Bull 58:1427–1435

Jin L, Chen F, Morrill C, Otto-Bliesner BL, Rosenbloom N (2012) Causes of early Holocene desertification in arid central Asia. Clim Dyn 38:1577–1591

Joos F, Spahni R (2008) Rates of change in natural and anthropogenic radiative forcing over the past 20,000 years. Proc Natl Acad Sci 105:1425–1430

Li Y, Yang S (2010) A dynamical index for the East Asian winter monsoon. J Clim 23:4255–4262

Li Y, Wang N, Chen H, Li Z, Zhou X, Zhang C (2012a) Tracking millennial-scale climate change by analysis of the modern summer precipitation in the marginal regions of the Asian monsoon. J Asian Earth Sci 58:78–87

Li Y, Wang N, Li Z, Zhang C, Zhou X (2012b) Reworking effects in the Holocene Zhuye Lake sediments: a case study by pollen concentrates AMS ^{14}C dating. Sci China Earth Sci 55:1669–1678

Liu TS, Ding ZL (1993) Stepwise coupling of monsoon circulations to global ice volume variations during the late Cenozoic. Glob Planet Change 7:119–130

Liu TS, Ding ZL (1998) Chinese loess and the paleomonsoon. Annu Rev Earth Planet Sci 26:111–145

Liu X, Dong H, Yang X, Herzschuh U, Zhang E, Stuut JBW, Wang Y (2009a) Late Holocene forcing of the Asian winter and summer monsoon as evidenced by proxy records from the northern Qinghai–Tibetan Plateau. Earth Planet Sci Lett 280:276–284

Liu Z, Otto-Bliesner BL, He F, Brady EC, Tomas R, Clark PU, Carlson AE, Lynch-Stieglitz J, Curry W, Brook E, Erickson D, Jacob R, Kutzbach J, Cheng J (2009b) Transient simulation of last deglaciation with a new mechanism for Bølling-Allerød warming. Science 325:310–314

Lu H, Zhang FQ, Liu X, Duce RA (2004) Periodicities of palaeoclimatic variations recorded by loess-paleosol sequences in China. Quat Sci Rev 23:1891–1900

Morrill C, Overpeck JT, Cole JE, Liu K, Shen C, Tang L (2006) Holocene variations in the Asian monsoon inferred from the geochemistry of lake sediments in central Tibet. Quat Res 65:232–243

Morrill C, Wagner AJ, Otto-Bliesner BL, Rosenbloom N (2011) Evidence for significant climate impacts in monsoonal Asia at 8.2 ka from multiple proxies and model simulations. J Earth Environ 2:427–441

Otto-Bliesner BL, Brady EC, Clauzet G, Tomas R, Levis S, Kothavala Z (2006) Last glacial maximum and Holocene climate in CCSM3. J Clim 19:2526–2544

Peltier WR (2004) Global glacial isostasy and the surface of the ice-age Earth: the ICE-5G (VM2) model and GRACE. Annu Rev Earth Planet Sci 32:111–149

Prins MA, Postma G, Weltje G (2000) Controls on terrigenous sediment supply to the Arabian Sea during the late Quaternary: the Makran continental slope. Mar Geol 169:351–371

Pye K (1995) The nature, origin and accumulation of loess. Quat Sci Rev 14:653–667

Rea DK, Leinen M, Janecek TR (1985) Geologic approach to the long-term history of atmospheric circulation. Science 227:721–725

Shi ZG, Liu XD, Sun YB, An ZS, Liu Z, Kutzbach J (2011) Distinct responses of East Asian summer and winter monsoons to astronomical forcing. Clim Past 7:1363–1370

Sun DH, Bloemendal J, Rea DK, Vandenberghe J, Jiang FC, An ZS, Su RX (2002) Grain-size distribution function of polymodal sediments in hydraulic and aeolian environments, and numerical partitioning of the sedimentary components. Sediment Geol 152:263–277

Sun DH, Bloemendal J, Rea DK, An ZS, Vandenberghe J, Lu HY, Su RX, Liu TS (2004) Bimodal grain-size distribution of Chinese loess, and its palaeoclimatic implications. Catena 55:325–340

Sun DH, Su R, Bloemendal J, Lu H (2008) Grain-size and accumulation rate records from Late Cenozoic aeolian sequences in northern China: implications for variations in the East Asian winter monsoon and westerly atmospheric circulation. Palaeogeogr Palaeoclimatol Palaeoecol 264:39–53

Sun Y, Clemens SC, Morrill C, Lin X, Wang X, An Z (2012) Influence of Atlantic meridional overturning circulation on the East Asian winter monsoon. Nat Geosci 5:46–49

Tian J, Huang EQ, Pak DK (2010) East Asian winter monsoon variability over the last glacial cycle: insights from a latitudinal sea-surface temperature gradient across the South China Sea. Palaeogeogr Palaeoclimatol Palaeoecol 292:319–324

Wang B, Lin H (2002) Rainy season of the Asian-Pacific summer monsoon. J Clim 15:386–396

Wang B, Wu R, Fu X (2000) Pacific-East Asia teleconnection: how does ENSO affect East Asian climate? J Clim 13:1517–1536

Wang L, Lu HY, Liu JQ, Gu ZY, Mingram J, Chu GQ, Li JJ, Rioual P, Negendank JFW, Han JT, Liu TS (2008) Diatom-based inference of variations in the strength of Asian winter monsoon winds between 17,500 and 6000 calendar years BP. J Geophys Res Atmos. 113(D21) doi:10.1029/2008JD010145

Wang L, Li J, Lu H, Gu Z, Rioual P, Hao Q, Mackay AW, Jiang W, Cai B, Xu B, Han J, Chu G (2012) The East Asian winter monsoon over the last 15, 000 years: its links to high-latitudes and tropical climate systems and complex correlation to the summer monsoon. Quat Sci Rev 32:131–142

Webster PJ, Magana VO, Palmer TN (1998) Monsoon: process, predictability, and the prospects for forecast. J Geophys Res 103:14454–14510

Weltje GJ, Prins M (2007) Genetically meaningful decomposition of grainsize distributions. Sediment Geol. doi:10.1016/j.sedgeo.2007.03.007

Wu BY, Huang RH, Wang J (2002) Possible impacts of winter Arctic Oscillation on Siberian high, the East Asian winter monsoon and sea–ice extent. Adv Atmos Sci 19:297–320

Xiao JL, Porter SC, An ZS, Kumai H, Yoshikawa S (1995) Grain-size of quartz as an indicator of winter monsoon strength on the Loess

Plateau of central China during the last 130,000–yr. Quat Res 43:22–29

Xiao JL, Nakamura T, Lu H, Zhang G (2002) Holocene climate changes over the desert/loess transition of north-central China. Earth Planet Sci Lett 197:11–18

Xiao S, Li A, Jiang F, Li T, Huang P, Xu Z (2005) Recent 2000-year geological records of mud in the inner shelf of the East China Sea and their climatic implications. Chin Sci Bull 50:466–471

Yancheva G, Nowaczyk NR, Mingram J, Dulski P, Schettler G, Negendank JFW, Liu JQ, Sigman DM, Peterson LC, Haug GH (2007) Influence of the intertropical convergence zone on the East Asian monsoon. Nature 445:74–77

Yang SL, Ding ZL (2008) Advance–retreat history of the East-Asian summer monsoon rainfall belt over northern China during the last two glacial–interglacial cycles. Earth Planet Sci Lett 274:499–510

Yang S, Lau KM, Kim KM (2002) Variations of the East Asian jet stream and Asian-Pacific-American winter climate anomalies. J Clim 15:306–325

Yang X, Preusser F, Radtke U (2006) Late Quaternary environmental changes in the Taklamakan Desert, western China, inferred from OSL-dated lacustrine and Aeolian deposits. Quat Sci Rev 25:923–932

Yang X, Scuderi L, Paillou P, Liu Z, Li H, Ren X (2011) Quaternary environmental changes in the drylands of China—A critical review. Quat Sci Rev 30:3219–3233

Yu X, Zhou W, Liu Z, Kang Z (2011) Different patterns of changes in the Asian summer and winter monsoons on the eastern Tibetan Plateau during the Holocene. Holocene. doi:10.1177/0959683611400460

Yun KS, Seo KH, Ha KJ (2010) Interdecadal change in the relationship between ENSO and the Intraseasonal Oscillation in East Asia. J Clim 23:3599–3612

Zhang Y, Sperber K, Boyle J (1997) Climatology and interannual variation of the East Asian winter monsoon: results from the 1979–95 NCEP/NCAR reanalysis. Mon Weather Rev 125:2605–2619

Zhao SQ (1983) A new scheme for comprehensive physical regionalization in China. Acta Geogr Sin 38:1–10 (in Chinese)

Zhou BT, Zhao P (2009) Inverse correlation between ancient winter and summer monsoons in East Asia? Chin Sci Bull 54:3760–3767

Zhou W, Donahue DJ, Jull AJT (1997) Radiocarbon AMS dating of pollen concentrated from eolian sediments: implications for monsoon climate change since the late Quaternary. Radiocarbon 39:19–26

Zhou HY, Wang B, Guan HZ, Lai Y, You C, Wang JL, Yang H (2009) Constraints from strontium and neodymium isotopic ratios and trace elements on the sources of the sediments in Lake Huguang Maar. Quat Res 72:289–300